



# Enhanced visible light photocatalytic performance of a novel heterostructured $\text{Bi}_4\text{O}_5\text{Br}_2/\text{Bi}_{24}\text{O}_{31}\text{Br}_{10}/\text{Bi}_2\text{SiO}_5$ photocatalyst

Di Liu, Wenqing Yao, Jun Wang, Yanfang Liu, Mo Zhang, Yongfa Zhu\*

Department of Chemistry, Beijing Key Laboratory for Analytical Methods and Instrumentation, Tsinghua University, Beijing 100084, PR China

## ARTICLE INFO

### Article history:

Received 11 December 2014

Received in revised form 23 January 2015

Accepted 25 January 2015

Available online 23 February 2015

### Keywords:

O-rich BiOBr

$\text{Bi}_2\text{SiO}_5$

Ion exchange

Photocatalysis

Heterojunction

## ABSTRACT

A novel  $\text{Bi}_4\text{O}_5\text{Br}_2/\text{Bi}_{24}\text{O}_{31}\text{Br}_{10}/\text{Bi}_2\text{SiO}_5$  heterostructure photocatalyst was synthesized successfully by in situ ion exchange reaction using BiOBr microspheres as the starting material for the first time. The heterostructured semiconductor showed superior photocatalytic activity in visible light degradation of phenol compared to pure BiOBr and other reported Bi-based photocatalysts. The exceptional photocatalytic activity of the heterostructured system can be attributable to the well-aligned straddling band-gap structures which can promote the flow of charge carriers via the heterojunction, extended light absorbance and a large Brunauer–Emmett–Teller (BET) specific surface area. The present work also proves that engineering of heterojunctions with high matching of lattices and well-aligned straddling band-structures is a significantly efficient way to achieve photocatalysts with high photocatalytic activity.

© 2015 Elsevier B.V. All rights reserved.

## 1. Introduction

To realize full utilization of the solar energy, it is of great importance to further investigate of novel visible-light-driven photocatalysts. Recently, bismuth oxyhalides ( $\text{BiOX}$ ,  $X = \text{F}$ ,  $\text{Cl}$ ,  $\text{Br}$ ,  $\text{I}$ ) which possess broad ranged band gaps, unique layered structure and excellent stability are of considerable interests in visible-light-driven photocatalysts [1–7]. Especially for BiOBr, possessing a layered structure composed of an alternating arrangement of  $(\text{Bi}_2\text{O}_2)^{2+}$  slabs and double slabs of  $\text{Br}^-$ , has stimulated great research interest because of its relatively superior performance as a visible-light photocatalyst [8–11]. However, to put the application into practice, the photodegradation ability and the spectral response range of BiOBr need further improvement. Construction of a heterojunction with matching band structures is an outstanding approach to enhance the photocatalytic activity of the heterostructured semiconductor via significantly facilitating the separation of photo-generated carries [12,13]. So far, Many heterojunctions concerning BiOBr, such as  $\text{BiOI}/\text{BiOBr}$  [14,15],  $\text{Ag}/\text{AgBr}/\text{BiOBr}$  [12],  $\text{BiOBr}/\text{Bi}_2\text{WO}_6$  [16],  $\text{BiOBr}-\text{C}_3\text{N}_4$  [17,18],  $\text{BiOBr}/\text{hydrated bismuth oxide (BHO)}$  [19],  $\text{BiOBr}/\text{TiO}_2$  [20],  $\text{BiOBr}/\text{ZnFe}_2\text{O}_4$  [21] had been reported and exhibited enhanced photocatalytic activities. Therefore, the heterojunction of bismuth oxybromides sensitized hybrids is in urgent need. Recently,  $\text{Bi}_2\text{SiO}_5$  is also reported to be one

member of the Aurivillius family [22,23]. At the same time,  $\text{Bi}_2\text{SiO}_5$  which is composed of  $\text{SiO}_3^{2-}$  pyroxene file layers inserted between  $(\text{Bi}_2\text{O}_2)^{2+}$  layers [24] has a similar structure and a lower solubility to BiOBr. Therefore, it is feasible for BiOBr to partly transform into  $\text{Bi}_2\text{SiO}_5$  via a thermodynamically favored direction through the ion exchange reaction which allows the exchange between the component ions and the incoming species [12,25,26], and consequently the bismuth oxybromides/ $\text{Bi}_2\text{SiO}_5$  heterojunction can be obtained. To the best of our knowledge, heterostructured semiconductors consisting of bismuth oxybromides and  $\text{Bi}_2\text{SiO}_5$  have not yet been reported.

Hereby, our design strategy adopts the BiOBr microspheres as the starting materials to partially transform into a novel heterostructure between bismuth oxybromides and  $\text{Bi}_2\text{SiO}_5$ . Along with the increase in the amount of incoming ions, interesting morphological evolution was found through observation of the as-prepared products using electron microscopes. Moreover, the novel heterostructured photocatalyst possesses a large BET specific area, a narrowed band-gap and well-aligned straddling band-structures and consequently exhibits significantly enhanced photocatalytic activity in visible-light degradation of phenol.

## 2. Experimental

### 2.1. Materials preparation

All chemicals used were analytical-grade reagents without further purification. The synthesis of sacrificial template of BiOBr is

\* Corresponding author. Tel.: +86 10 6278 7601; fax: +86 10 6278 7601.  
E-mail address: [zhuyf@tsinghua.edu.cn](mailto:zhuyf@tsinghua.edu.cn) (Y. Zhu).

based on a modified method in the reported literature [27] and can be described as follows. Acetic acid (45 mL) and  $\text{Bi}(\text{NO}_3)_3 \cdot 5\text{H}_2\text{O}$  (14.55 g) were completely dissolved in 85 mL deionized water in a beaker and stirred for an appropriate time under room temperature until a clear, homogeneous solution was formed. Afterward, 40 mL deionized water containing 10.93 g CTAB was added to the above solution all at once, and the mixture was submitted to stir at room temperature for another 0.5 h. After the reaction was finished, the obtained precipitate (BiOBr) was washed with ethanol and deionized water for several times to remove the nonreactive species, and then dried in oven for subsequent use. To synthesize the heterostructured samples, in a typical reaction,  $\text{Na}_2\text{SiO}_3$  (0, 0.1 mmol, 0.2 mmol, 0.5 mmol, 1 mmol) was dissolved separately in 80 mL distilled water and stirred at room temperature for 10 min to obtain clear solutions. Then, the as-prepared BiOBr (1.22 g) was dispersed respectively in each of the above solutions with stirring. Each mixture was all stirred for 30 min under room temperature and then transferred into a 100 mL Teflon-lined autoclave, and heated at  $160^\circ\text{C}$  for 24 h. After reaction, the autoclave was cooled to room temperature naturally. The precipitates were collected by centrifugation, washed with deionized water and ethanol for several times, and finally dried in oven at  $80^\circ\text{C}$  for 10 h. Products with different adding amount of  $\text{Na}_2\text{SiO}_3$  ranging from 0 to 1 mmol were prepared according to this method and were marked as BiOBr, S-0.1, S-0.2, S-0.5, S-1, respectively. (The synthesis of pure  $\text{Bi}_2\text{SiO}_5$  was according to the above procedure with 4 mmol  $\text{Bi}(\text{NO}_3)_3 \cdot 5\text{H}_2\text{O}$  and 2 mmol  $\text{Na}_2\text{SiO}_3$  as the precursors and the solvent pH was adjusted to cal. 9 by 10% ammonia solution. The pure  $\text{Bi}_2\text{SiO}_5$  synthesized above was labeled as  $\text{Bi}_2\text{SiO}_5$ ).

Synthesis of control sample ( $\text{Bi}_2\text{MoO}_6$ ): deionized water (120 mL),  $\text{Na}_2\text{MoO}_4 \cdot 2\text{H}_2\text{O}$  (0.60 g, 2.5 mmol) and  $\text{Bi}(\text{NO}_3)_3 \cdot 5\text{H}_2\text{O}$  (2.43 g, 5 mmol) were placed into a 250 mL flask and then the pH of the mixed solution was adjusted to 6 with a NaOH solution (2 M) under stirring. The resulting precursor suspension was refluxed at  $100^\circ\text{C}$  for 12 h. After the reaction, the flask was cooled to room temperature naturally. The precipitates were collected by centrifugation, and washed with deionized water and ethanol for several times, and finally dried in oven at  $80^\circ\text{C}$  for 10 h.

## 2.2. Characterization

A Bruker D8 Advance X-ray diffractometer was used to gain analysis of X-ray diffraction (XRD) patterns. The sizes and morphologies of the as-prepared samples were collected through a LEO-1530 field emission Scanning Electron Microscope (SEM) and a HITACHI HT7700 transmission electron microscope (TEM). High-resolution transmission electron microscopy (HRTEM) images were acquired with JEOL JEM-2010F field emission transmission electron microscope with an accelerating voltage of 200 kV. Fourier transform infrared spectra (FT-IR) were taken with a Bruker VERTEX 700 spectrometer in the frequency range of  $4000\text{--}600\text{ cm}^{-1}$  with a resolution of  $4\text{ cm}^{-1}$ . Raman scattering (HORIBA HR800 confocal microscope Raman spectrometer) of the as-prepared samples were excited using an Ar-ion laser ( $514.5\text{ nm}$ ). All spectra were calibrated with respect to silicon wafer at  $520.7\text{ cm}^{-1}$ . The Brunauer-Emmett-Teller (BET) surface areas were measured using a micromeritics (ASAP 2010V5.02H) surface area analyzer. The samples were pretreated by degassing on orpтомatic 1900 Carlo Erba Instrument and then measured at 77 K to produce nitrogen adsorption and desorption isotherms. Diffuse reflectance spectra (DRS) of the as-prepared samples were recorded in the range of  $200\text{--}800\text{ nm}$  using a Hitachi U-3010 spectroscope. The photocurrent measurements were performed on an electrochemical workstation (CHI-660B, China). A 500 W Xe lamp (Institute for Electric Light Sources, Beijing) with a 420 nm cut-off filter provided the visible irradiation. A standard three-electrode cell with ITO/product sample as a working

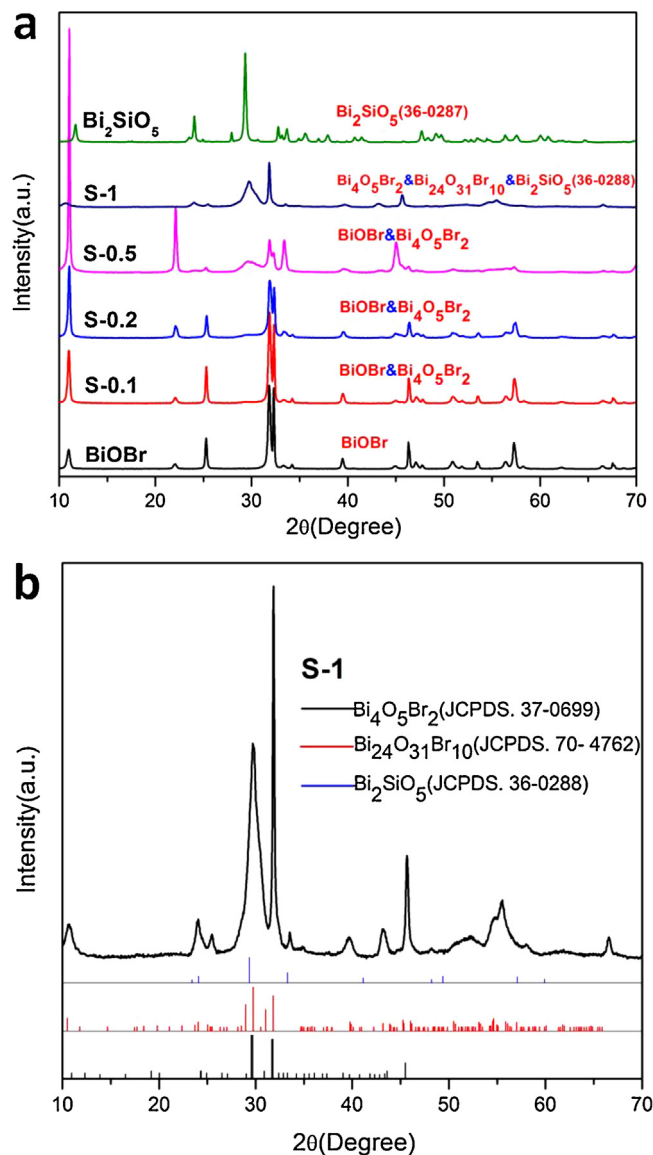


Fig. 1. XRD patterns of the as-prepared products (a) and S-1 (b).

electrode, a platinum wire as a counter electrode, and a standard calomel electrode (SCE) as reference electrode were used in photoelectric investigations, among which 0.1 M  $\text{Na}_2\text{SO}_4$  was the electrolyte solution. The photoelectric responses of the photocatalysts as light on and off were measured at 0.0 V. X-ray photoelectron spectroscopy (XPS) measurements were carried out in a PHI 5300 ESCA system with the energy of Ar ion beam at 1.0 keV and the beam voltage set at 3.0 kV.

ITO/product electrodes were prepared as follows: the as-prepared product (10 mg) was suspended in 1 mL of ethanol, and the obtained mixture was further dispersed by an ultrasound bath. Then, the slurry was dip-coated onto a  $2\text{ cm} \times 4\text{ cm}$  indium-tin oxide (ITO) glass electrode. Electrodes were subsequently calcined at  $150^\circ\text{C}$  for 5 h. All investigated electrodes were of similar thickness.

## 2.3. Photocatalytic experiments

In this work, photo-degradation of phenol under visible light irradiation ( $\lambda \geq 420\text{ nm}$ ) was adopted to evaluate the photocatalytic performance of the as-prepared samples. A 500 W Xe lamp (Institute for Electric Light Sources, Beijing) with a 420 nm cut off filter

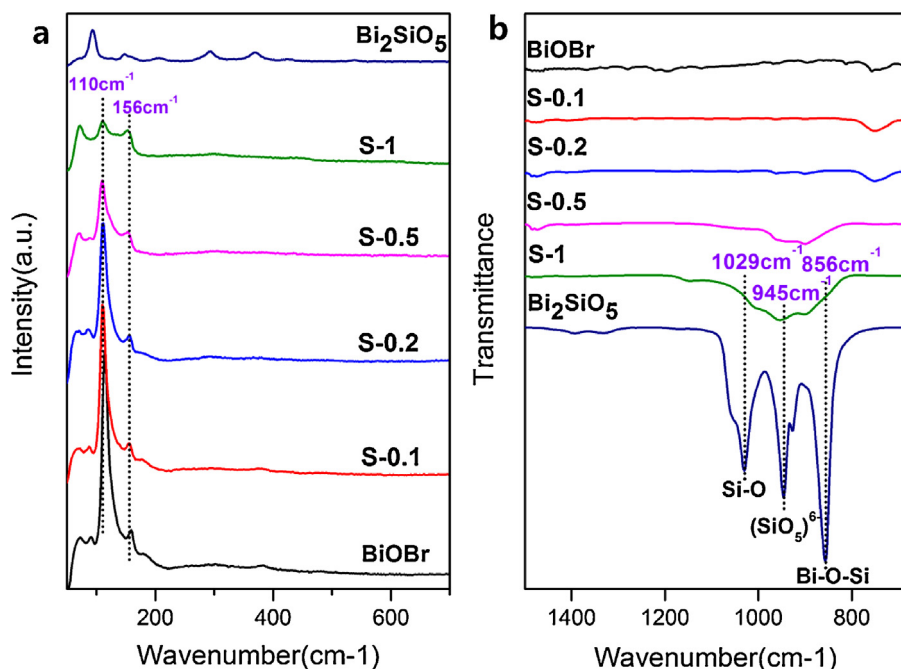


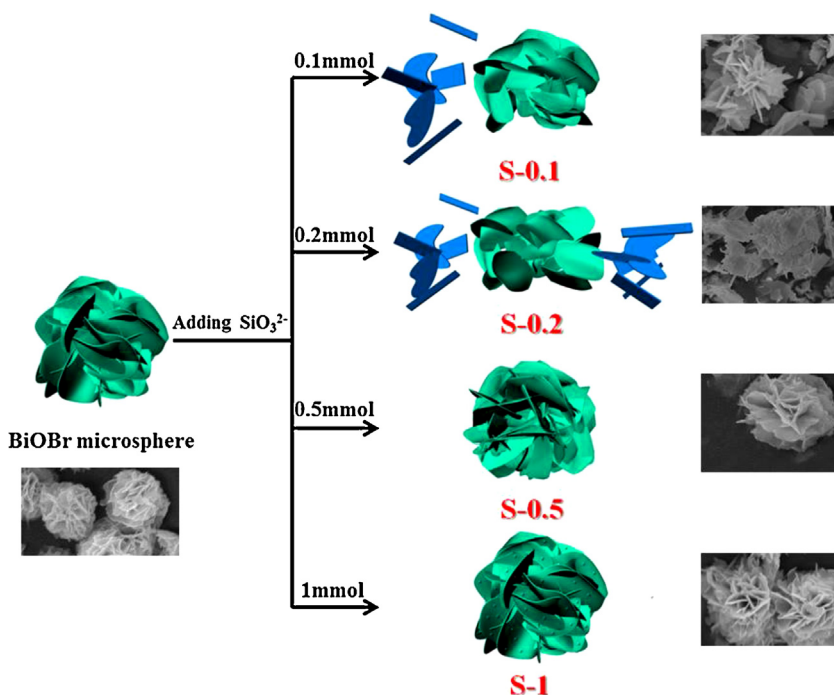
Fig. 2. Raman (a) and FT-IR (b) spectra of the as-prepared products.

was used to provide the visible light irradiation, and the average visible light intensity was  $38 \text{ mW cm}^{-2}$ . Before the light irradiation, a suspension of 30 mg of photocatalyst in 50 mL of phenol aqueous solution (5 mg/L) was first ultrasonic dispersed in dark for 15 min and then magnetically stirred for 1 h. At certain time intervals, a suspension (2 mL) was extracted and centrifugated to remove the photocatalyst. The degradation process was monitored by HPLC analysis with the mobile phase containing methanol and water (60%: 40%), UV detector set at 270 nm and the flow rate set at 1 mL/min.

### 3. Results and discussions

#### 3.1. Formation of the heterostructure

As shown in Fig. 1, the X-ray diffraction (XRD) patterns are provided to reveal the crystallinity and phase structures of the as-prepared samples. Table 1 supplies the phase composition and atomic ratio (Bi:O:Br) of new phase in each product. It can be found from Fig. 1a that when the hydrothermal reactions were performed without adding  $\text{Na}_2\text{SiO}_3$ , the diffraction peak of the



Scheme 1. Model diagram of the as-prepared products at different adding amount of  $\text{SiO}_3^{2-}$ .

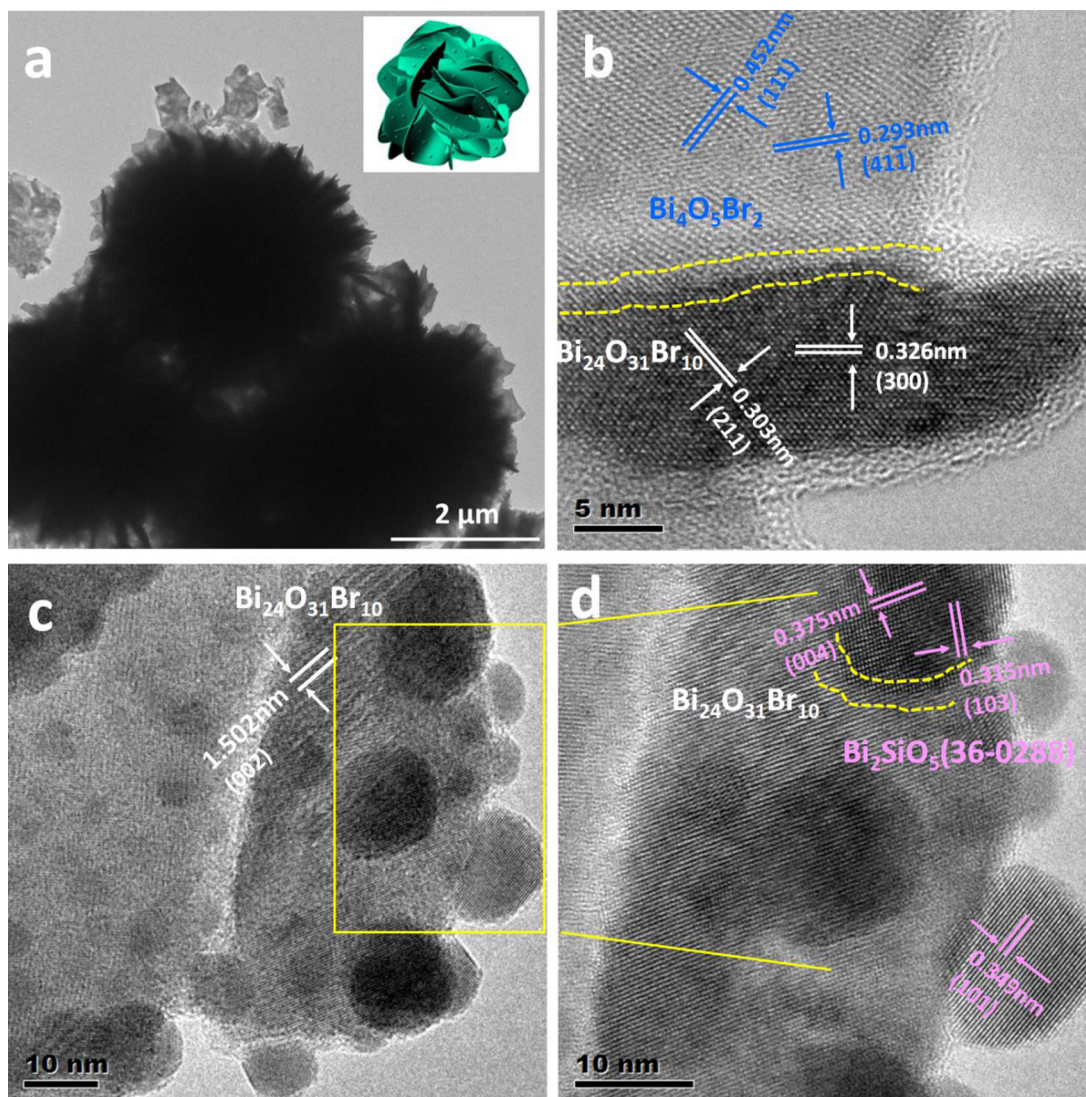


Fig. 3. TEM image (a) and HRTEM images (b–d) of S-1.

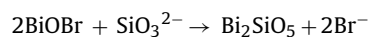
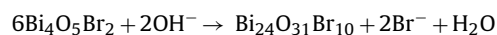
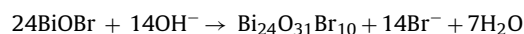
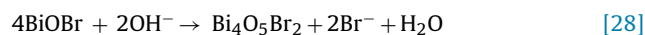
Table 1

Phase composition and ratio of Bi:O:Br in the new phase for the as-prepared products.

Sample	Phase composition	Ratio of Bi:O:Br in the new phase
BiOBr	BiOBr	24:24:24
S-0.1	BiOBr&Bi <sub>4</sub> O <sub>5</sub> Br <sub>2</sub>	24:30:12
S-0.2	BiOBr&Bi <sub>4</sub> O <sub>5</sub> Br <sub>2</sub>	24:30:12
S-0.5	BiOBr&Bi <sub>4</sub> O <sub>5</sub> Br <sub>2</sub>	24:30:12
S-1	Bi <sub>4</sub> O <sub>5</sub> Br <sub>2</sub> &Bi <sub>24</sub> O <sub>31</sub> Br <sub>10</sub> &Bi <sub>2</sub> SiO <sub>5</sub>	24:31:10

sample (BiOBr) could be well indexed as BiOBr with a tetragonal phase (JCPDS No. 09-0393). However, it was found that the diffraction peaks of the as-prepared products underwent obvious changes after the addition of Na<sub>2</sub>SiO<sub>3</sub>. The higher O:Br ratio was observed with more SiO<sub>3</sub><sup>2-</sup> addition in the obtained product, as shown in Table 1, Bi<sub>2</sub>SiO<sub>5</sub> appeared only when the adding amount of SiO<sub>3</sub><sup>2-</sup> is equal to or greater than 1 mmol. When the adding amount of SiO<sub>3</sub><sup>2-</sup> was increased to 1.5 mmol, the product fully transformed into Bi<sub>2</sub>SiO<sub>5</sub> with a decreased visible light photocatalytic activity, thus sample S-1.5 was not taken into discussion in this work. The XRD patterns of samples S-0.1–S-0.5 showed the coexistence of BiOBr (JCPDS card No. 09-0393) and Bi<sub>4</sub>O<sub>5</sub>Br<sub>2</sub> (JCPDS card No. 37-0699). As shown in Fig. 1b, S-1 was found to contain three phases:

Bi<sub>4</sub>O<sub>5</sub>Br<sub>2</sub> (JCPDS card No. 37-0699), Bi<sub>24</sub>O<sub>31</sub>Br<sub>10</sub> (JCPDS card No. 70-4762) and Bi<sub>2</sub>SiO<sub>5</sub> (JCPDS card No. 36-0288). It is known that the hydrolysis of Na<sub>2</sub>SiO<sub>3</sub> would make the solution alkaline. As previously reported, O-rich/Br-poor bismuth oxybromides can be obtained from BiOBr through OH<sup>-</sup> gradually replacing Br<sup>-</sup> under the basic reaction condition [28]. As a result, with increasing addition of SiO<sub>3</sub><sup>2-</sup>, BiOBr first evolved into Bi<sub>4</sub>O<sub>5</sub>Br<sub>2</sub> and then gradually transformed into Bi<sub>24</sub>O<sub>31</sub>Br<sub>10</sub> through OH<sup>-</sup> substituting Br<sup>-</sup>. Only when the adding amount of SiO<sub>3</sub><sup>2-</sup> is high enough, can bismuth oxybromides evolve into a more stable phase (Bi<sub>2</sub>SiO<sub>5</sub>) through SiO<sub>3</sub><sup>2-</sup> substituting Br<sup>-</sup>. The reaction process can be described as follows:



In order to get better knowledge of the impact of the adding amount of SiO<sub>3</sub><sup>2-</sup> on the products, the morphology changes of the as-prepared products were also studied.

As shown in Fig. S1, the original morphology of the sacrificial template (BiOBr) is flower-like microsphere with great uniformity. After adding  $\text{SiO}_3^{2-}$  into the solution (S-0.1), some pieces and irregular flower-like microspheres appeared. Further increasing the  $\text{SiO}_3^{2-}$  (S-0.2), more scattered pieces and much more irregular microspheres were obtained. However, flower-like microspheres assembled by nanosheets can be found again in sample S-0.5 and S-1, suggesting that the different kind of anion exchange would result in interesting morphology evolution. The model diagram of the morphology evolution with increasing addition of  $\text{SiO}_3^{2-}$  is provided in Scheme 1. It can be concluded that the anion exchange between  $\text{OH}^-$  and  $\text{Br}^-$  would generate the O-rich bismuth oxybromides with fragmentary sheet-like morphologies, while the anion exchange between  $\text{SiO}_3^{2-}$  and  $\text{Br}^-$  could result in product restoring the shape of sacrificial template. It was reported that the composition and structure of bismuth oxybromides will have great influences on their optical, electronic, and other physicochemical properties [29]. Then, the optical and energy band structural features of the as-prepared products were discussed in the following.

BiOBr crystallizes in the tetragonal structure of P4/nmm space group and has three kinds of Raman active modes ( $A_{1g}$ ,  $B_{1g}$  and  $E_g$ ). As shown in Fig. 2a, the strong band at  $110\text{ cm}^{-1}$  could be assigned to  $A_{1g}$  internal Bi–Br stretching mode. The band at  $156\text{ cm}^{-1}$  could be attributed to the  $E_g$  internal Bi–Br stretching mode [30,31]. It can be seen that these two characteristic vibrations of BiOBr decreased gradually with increasing addition of  $\text{SiO}_3^{2-}$ , indicating the growing transformation degree of BiOBr. Fourier transform infrared spectra (FT-IR) results are shown in Fig. 2b. Based on previously reports [32–34], the peaks located around  $856\text{ cm}^{-1}$ ,  $945\text{ cm}^{-1}$  and  $1029\text{ cm}^{-1}$  belong to the stretching vibration mode of the Bi–O–Si bonds, the isolated  $(\text{SiO}_5)^{6-}$  groups and the Si–O bond, respectively. As shown in Fig. 2b, with an increased adding amount of  $\text{SiO}_3^{2-}$ , the intensity of these three peaks enhanced obviously. Therefore, this result further confirmed the formation of Bi–O–Si and Si–O bonds at larger adding amount of  $\text{SiO}_3^{2-}$ .

The transmission electron microscope (TEM) and high-resolution transmission electron microscopy (HRTEM) images of S-1 are shown in Fig. 3. Sample S-1 is composed of two different structures: flower-like microsphere assembled by stacking nanosheets was the main component and individual nanoplate was the minor component (Fig. 3a). The TEM and HRTEM results confirmed the successful formation of heterostructures containing three phases without shape collapse of the sacrificial template of BiOBr. A strong and stable heterojunction relies on a high matching degree of lattices of the components. A HRTEM image of an individual nanosheet is presented in Fig. 3b. Careful observation reveals that the lattice spacing of  $0.452$  and  $0.293\text{ nm}$  correspond to  $(111)$  and  $(411^-)$  planes of  $\text{Bi}_4\text{O}_5\text{Br}_2$ , and the lattice spacing of  $0.303$  and  $0.326\text{ nm}$  correspond to  $(211)$  and  $(300)$  planes of  $\text{Bi}_{24}\text{O}_{31}\text{Br}_{10}$ . From view of the yellow line circled part in Fig. 3b, the continuity in lattice can be clearly seen between  $\text{Bi}_4\text{O}_5\text{Br}_2$  and  $\text{Bi}_{24}\text{O}_{31}\text{Br}_{10}$ . Fig. 3c shows the clear lattice spacing of  $1.502\text{ nm}$  which can be attributed to the d-spacing between  $(002)$  planes of  $\text{Bi}_{24}\text{O}_{31}\text{Br}_{10}$ . The enlarged image of the area labeled by a rectangle in Fig. 3c is shown in Fig. 3d, the lattice fringes have a clear separation of  $0.375$ ,  $0.315$  and  $0.349\text{ nm}$  which correspond to d-spacing of the  $(004)$ ,  $(103)$  and  $(101)$  planes of  $\text{Bi}_2\text{SiO}_5$ , respectively. It is noteworthy that the nano-spheres which are easy to differentiate from the surrounding sheets where they were embedded are attributed to  $\text{Bi}_2\text{SiO}_5$ . From view of the ambiguous nano-spheres with poor formation in Fig. 3c, it can be concluded that these nano-spheres should be evolved from the surrounding sheets which corresponds to the phase of  $\text{Bi}_{24}\text{O}_{31}\text{Br}_{10}$ . Importantly, Fig. 3c,d reveal the intimate connection and continuity in lattice between  $\text{Bi}_{24}\text{O}_{31}\text{Br}_{10}$  and  $\text{Bi}_2\text{SiO}_5$ , further indicating the successful formation of the three phases heterostruc-

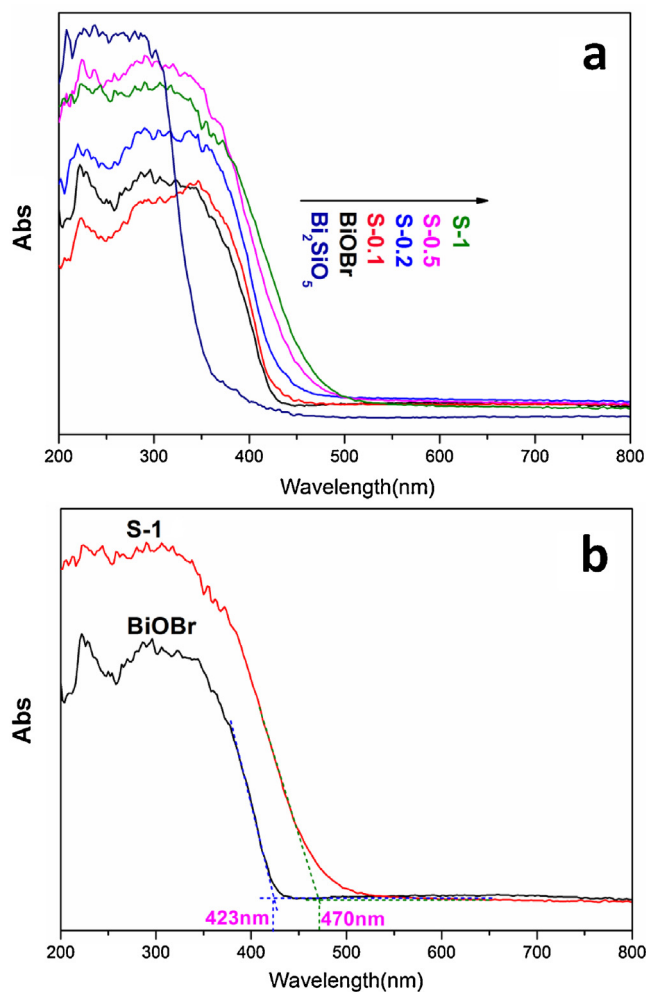


Fig. 4. DRS spectra of the as-prepared products (a) and BiOBr&S-1 (b).

tures. At the same time, the lattice-match between two materials was also supposed to play a vital role in the phase evolution.

As is known that the surface area would have an effect on photo-reactivity, then the BET surface area of the samples (BiOBr, S-0.1, S-0.2, S-0.5, S-1) were measured from  $\text{N}_2$  isotherms and were found to be  $10.6735$ ,  $5.4157$ ,  $7.9101$ ,  $15.7379$  and  $18.2082\text{ m}^2\cdot\text{g}^{-1}$  (Fig. S2), respectively. It can be seen that when the adding amount of  $\text{SiO}_3^{2-}$  was increased to  $1\text{ mmol}$ , the obtained sample of S-1 with hierarchical structure shows the largest specific surface area. A larger BET surface area is supposed to obtain a better photocatalytic performance by providing more active sites for the photochemical reaction.

### 3.2. Electronic structure

The optical properties of the as-prepared samples were investigated through the diffuse reflectance spectra (DRS) analysis. It can be seen from Fig. 4 that the absorption edges of the samples showed red shifts with increasing  $\text{SiO}_3^{2-}$ . The band gaps ( $E_g$ ) of the samples were calculated from the onsets of the absorption edges using the formula  $\lambda_g = 1239/E_g$ , where  $\lambda_g$  is the band-gap wavelength. The estimated band gaps are  $2.81$  and  $2.64\text{ eV}$  for BiOBr and S-1 based on the calculations of the DRS results. The substantial redshift of S-1 relative to BiOBr indicates that S-1 would have an obviously extended spectral response.

As mentioned above, the valence band composition and position of bismuth oxybromides can be tuned by the O: Br ratio

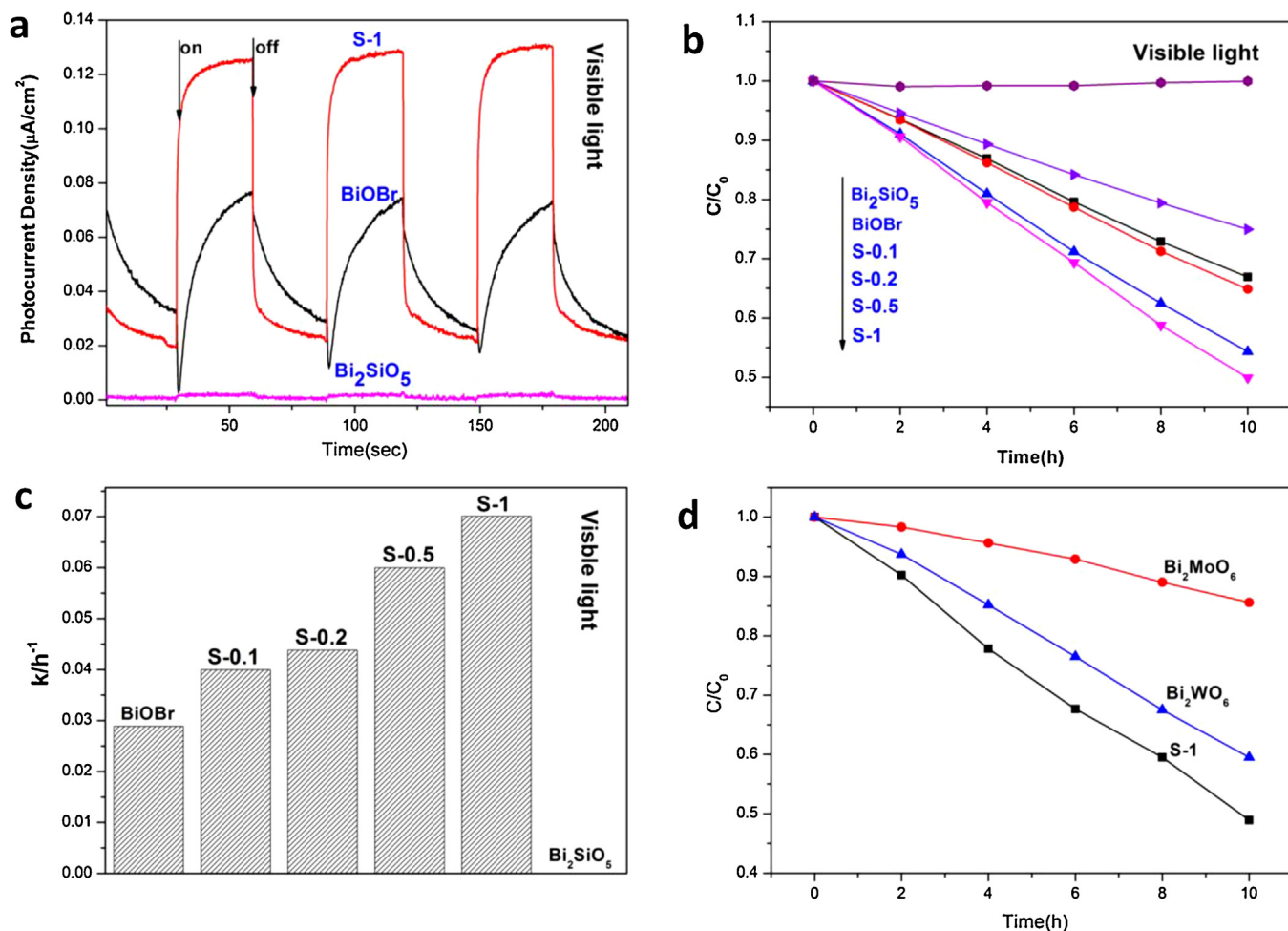


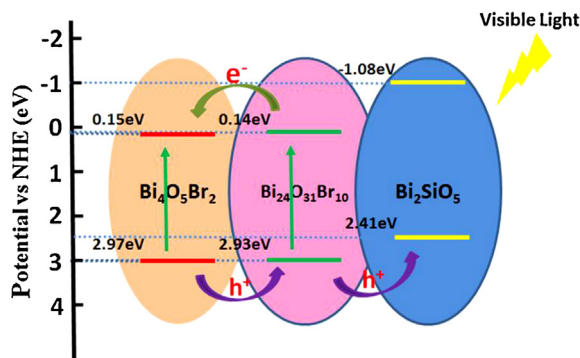
**Fig. 5.** The photocurrent of the as-prepared products electrodes under visible-light irradiation ( $\lambda \geq 420$  nm) (a), photocatalytic degradation ratio on phenol by the as-prepared products under visible-light irradiation ( $\lambda \geq 420$  nm) (b), Degradation rate constant  $k$  calculated from b (c), Comparison between S-1 and other reported Bi-based photocatalysts ( $Bi_2MoO_6$  and  $Bi_2WO_6$ ) in the photo-degradation of phenol under visible light irradiation (d).

[29]. X-ray photoelectron spectroscopy (XPS) is a useful testing technique to study the electronic structure of solids. The electronic structures of BiOBr and  $Bi_2SiO_5$  are investigated by valence band spectra of XPS (Fig. S3). Valence band X-ray photoelectron spectroscopy (VB-XPS) can directly probe the total density of the state (DOS) distribution in the valence band and thus has been widely used to investigate the VB top of the semiconductor [35]. Here, extra electronic states above the valence band of BiOBr and  $Bi_2SiO_5$  were investigated through VB-XPS spectra. Difference between the valence band of these two samples has been revealed by comparison in the range of binding energy [35] =  $-1-10$  eV (Fig. S3). The VB top of BiOBr and  $Bi_2SiO_5$  was found to be 1.53 eV, and 2.09 eV vs vacuum level, respectively.  $E_g$  is the band gap energy of the semiconductor; and  $E_{CBM}$  can be determined by  $E_{VBM} = E_{CBM} + E_g$ . Then, through the result of XPS valence band spectra and calculation of band gap energy  $E_g$ , the conduction band (CB) and valence band (VB) edge potentials of  $Bi_2SiO_5$  were estimated to be  $-1.08$  and  $2.41$  eV (vs NHE), respectively. The values used for calculating the CBM and VBM potentials of BiOBr and  $Bi_2SiO_5$  are listed in Table S1. According to the previous reports, the VB of BiOX is dominated by both O 2p and X np ( $n = 3, 4, 5$  and  $X = Cl, Br, I$ , respectively) states, while its CB is mainly governed by Bi 6p states. Importantly, in the O-rich BiOX system, the O 2p states would stand for much more portions than X np in VB compared to BiOX, and hence the band gap energies of O-rich BiOX become closer to  $Bi_2O_3$  [29,36]. Based on empirical equation and the electronegativity of semiconductors, the band positions for  $Bi_4O_5Br_2$  and  $Bi_{24}O_{31}Br_{10}$  were estimated to

be CB:  $0.15$  eV–VB:  $2.97$  eV and CB:  $0.14$  eV–VB:  $2.93$  eV vs NHE, respectively [29]. Band calculations elucidate that the three phases in the ternary heterojunction have well-aligned straddling band potentials, which consequently promotes the transfer and separation of the photo-generated electrons–holes. Detailed discussions are provided in the following part.

### 3.3. Photocatalytic performance

The  $e^- - h^+$  separation efficiency is known to be a decisive factor influencing the photocatalytic reaction [37]. Fig. 5a shows the transient photocurrent response of ITO/product electrodes in several on-off cycles under visible light irradiation. It can be found that S-1 displays the highest photocurrent, indicating its highly enhanced separation and transfer efficiency of photo-generated  $e^- - h^+$  [38]. For the photocatalytic reaction, dark absorption test was conducted before light irradiation. It can be seen from Fig. S4 that adsorption equilibrium was reached for all the catalysts at 20 min, and the adsorption quantity for all the catalysts are very low, and thus can be ignored. Then, Fig. 5b and c shows the photocatalytic degradation of phenol by the as-prepared products under visible light irradiation. In addition, HPLC chromatograms (S-1) monitoring the photodegradation process of phenol at interval times under visible light irradiation are provided in Fig. S5, revealing the continuous degradation of phenol along with irradiation time. Along with the increase of  $SiO_3^{2-}$ , the photocatalytic rate constant of the as-prepared samples also shows obvious increase. When the adding



**Scheme 2.** Schematic illustration of the band-gap structure and possible flow of charge carriers through the ternary heterostructure under visible light irradiation.

amount of  $\text{SiO}_3^{2-}$  reaches 1 mmol, the apparent rate constant  $k$  is ca. 2.5 times as high as that of pure  $\text{BiOBr}$ . In addition, a parallel comparison with other reported Bi-based photocatalysts [39] had been conducted. The result shown in Fig. 5d indicates that S-1 not only possesses an enhanced photocatalytic activity by comparison with the sacrificial template of  $\text{BiOBr}$ , but also is superior to other common Bi-based photocatalysts in the photo-degradation of phenol under the visible light irradiation. It is known to us that the light utilization could be enhanced by introducing a visible-light driven component in a heterostructure. In the ternary heterojunction,  $\text{Bi}_4\text{O}_5\text{Br}_2$  and  $\text{Bi}_{24}\text{O}_{31}\text{Br}_{10}$  both own narrower band gaps than  $\text{BiOBr}$ , thus they can absorb much more long-wavelength lights and enhance the utilization of light. In the view of electronic structure, the band potentials of  $\text{Bi}_4\text{O}_5\text{Br}_2$ ,  $\text{Bi}_{24}\text{O}_{31}\text{Br}_{10}$  and  $\text{Bi}_2\text{SiO}_5$  are compatible to form a heterojunction with a well-aligned straddling band upon their intimate contact. This heterojunction can benefit charge transfer significantly. On the one hand, the photo-generated electrons in the CB of  $\text{Bi}_{24}\text{O}_{31}\text{Br}_{10}$  can easily migrate to the CB of  $\text{Bi}_4\text{O}_5\text{Br}_2$ . On the other hand, holes formed in the VB of  $\text{Bi}_4\text{O}_5\text{Br}_2$  can readily transfer to the VB of  $\text{Bi}_{24}\text{O}_{31}\text{Br}_{10}$ . Similar facilitated transfer of the holes from the VB of  $\text{Bi}_{24}\text{O}_{31}\text{Br}_{10}$  to that of  $\text{Bi}_2\text{SiO}_5$  also happens. In this manner, long-lived reactive photo-charges can be yielded and thus the enhanced charge separation at the interface of the heterojunction can be achieved. The separation and transport of photo-induced carriers upon the interface of mixed ternary heterojunction is shown in Scheme 2. As for the surface photochemical reaction, photo-catalyst with a large specific surface area can provide more active sites for the photochemical reaction and then promotes the diffusion and mass transportation of the pollutants [40]. Thereby, the higher BET specific surface area of this ternary heterojunction would also make some contribution to the enhanced photocatalytic activity. Since the differences between the BET specific areas of the as-prepared products are not very much obvious (such as S-0.5 and S-1), we believed that the enhanced light utilization due to the existence of components with narrower band-gaps and the enhanced charge separation ability due to the well-aligned straddling band-structures would make the main contribution to the photocatalytic activity.

The durability is also an important factor for photocatalysts to meet the requirement in practical application. The catalyst recovered from the 1st cycle is reused to the second cycle and the same is continued up to 4 cycles. In the case of sample S-1, the photodegradation rate of 4 rounds continuous recycle photodegradation test is 49.1%, 44.2%, 37.1%, 33.5% respectively (Fig. S6), indicating a good durability of photocatalytic performance.

#### 4. Conclusion

In summary, a novel heterojunction of  $\text{Bi}_4\text{O}_5\text{Br}_2/\text{Bi}_{24}\text{O}_{31}\text{Br}_{10}/\text{Bi}_2\text{SiO}_5$  has been achieved through an

in situ ion exchange method. The successful formation of the heterojunction between bismuth oxybromides with  $\text{Bi}_2\text{SiO}_5$  could be attributed to their close structural similarity, thermo-dynamically allowance and high matching degree in lattices. The novel heterostructured photocatalyst involving a well-aligned straddling band upon their intimately contacted interfaces exhibits remarkable photocatalytic performance in visible light photodegradation of phenol, which is 2.5 times as high as that of pure  $\text{BiOBr}$ . The highly enhanced photocatalytic activity of the heterostructure can be ascribed to (1) the enhanced light utilization due to the existence of components with narrower band-gaps, (2) the evidently enhanced charge separation ability due to the well-aligned straddling band-structures, (3) the large specific surface area due to its hierarchical structure, which can give rise to abundant active sites for photocatalytic reaction. The research could be conducive to the design of new heterostructured photocatalysts with significantly improved photocatalytic performance.

#### Acknowledgments

This work was financially supported by National Basic Research Program of China (973 Program) (2013CB632403), National High Technology Research and Development Program of China (2012AA062701), National Natural Science Foundation of China (21373121).

#### Appendix A. Supplementary data

Supplementary data associated with this article can be found, in the online version, at <http://dx.doi.org/10.1016/j.apcatb.2015.01.037>.

#### References

- [1] W. Su, J. Wang, Y. Huang, W. Wang, L. Wu, X. Wang, P. Liu, *Scripta Mater.* 62 (2010) 345–348.
- [2] K.-L. Zhang, C.-M. Liu, F.-Q. Huang, C. Zheng, W.-D. Wang, *Appl. Catal. B* 68 (2006) 125–129.
- [3] H. An, Y. Du, T. Wang, C. Wang, W. Hao, J. Zhang, *Rare Metals* 27 (2008) 243–250.
- [4] X. Lin, T. Huang, F. Huang, W. Wang, J. Shi, *J. Phys. Chem. B* 110 (2006) 24629–24634.
- [5] W. Wang, F. Huang, X. Lin, *Scripta Mater.* 56 (2007) 669–672.
- [6] C. Wang, C. Shao, Y. Liu, L. Zhang, *Scripta Mater.* 59 (2008) 332–335.
- [7] J. Zhang, F. Shi, J. Lin, D. Chen, J. Gao, Z. Huang, X. Ding, C. Tang, *Chem. Mater.* 20 (2008) 2937–2941.
- [8] X. Zhang, Z. Ai, F. Jia, L. Zhang, *J. Phys. Chem. C* 112 (2008) 747–753.
- [9] J. Xu, W. Meng, Y. Zhang, L. Li, C. Guo, *Appl. Catal. B* 107 (2011) 355–362.
- [10] M.A. Gondal, X. Chang, M.A. Ali, Z.H. Yamani, Q. Zhou, G. Ji, *Appl. Catal. A* 397 (2011) 192–200.
- [11] H. Cheng, B. Huang, Z. Wang, X. Qin, X. Zhang, Y. Dai, *Eur. J. Chem.* 17 (2011) 8039–8043.
- [12] H. Cheng, B. Huang, P. Wang, Z. Wang, Z. Lou, J. Wang, X. Qin, X. Zhang, Y. Dai, *Chem. Commun.* 47 (2011) 7054–7056.
- [13] A. Hameed, T. Montini, V. Gombac, P. Fornasiero, *J. Am. Chem. Soc.* 130 (2008) 9658–9659.
- [14] J. Cao, B. Xu, B. Luo, H. Lin, S. Chen, *Catal. Commun.* 13 (2011) 63–68.
- [15] W. Wang, F. Huang, X. Lin, J. Yang, *Catal. Commun.* 9 (2008) 8–12.
- [16] Y. Li, Y. Liu, J. Wang, E. Uchaker, Q. Zhang, S. Sun, Y. Huang, J. Li, G. Cao, *J. Mater. Chem. A* 1 (2013) 7949–7956.
- [17] J. Fu, Y. Tian, B. Chang, F. Xi, X. Dong, *J. Mater. Chem.* 22 (2012) 21159–21166.
- [18] L. Ye, J. Liu, Z. Jiang, T. Peng, L. Zan, *Appl. Catal. B* 142–143 (2013) 1–7.
- [19] S. Shenawi-Khalil, V. Uvarov, S. Fronton, I. Popov, Y. Sasson, *J. Phys. Chem. C* 116 (2012) 11004–11012.
- [20] X. Cao, Z. Lu, L. Zhu, L. Yang, L. Gu, L. Cai, J. Chen, *Nanoscale* 6 (2014) 1434–1444.
- [21] L. Kong, Z. Jiang, T. Xiao, L. Lu, M.O. Jones, P.P. Edwards, *Chem. Commun.* 47 (2011) 5512–5514.
- [22] X.-J. Dai, Y.-S. Luo, S.-Y. Fu, W.-Q. Chen, Y. Lu, *Solid State Sci.* 12 (2010) 637–642.
- [23] E.N. Voskresenskaya, L.I. Kurteeva, V.P. Zhereb, A. Anshits, G. Catal. Today 13 (1992) 599–602.
- [24] S. Georges, F. Goutenoire, P. Lacorre, *J. Solid State Chem.* 179 (2006) 4020–4028.
- [25] D.H. Son, S.M. Hughes, Y.D. Yin, A.P. Alivisatos, *Science* 306 (2004) 1009–1012.

- [26] P. Wang, B. Huang, X. Qin, X. Zhang, Y. Dai, J. Wei, M.-H. Whangbo, *Angew. Chem. Int. Ed.* 47 (2008) 7931–7933.
- [27] G. Hani, Y. Sasson, *ACS Catalysis* 3 (2013) 186–191.
- [28] H. Deng, J. Wang, Q. Peng, X. Wang, Y. Li, *Chem. Eur. J.* 11 (2005) 6519–6524.
- [29] X. Xiao, C. Liu, R. Hu, X. Zuo, J. Nan, L. Li, L. Wang, *J. Mater. Chem.* 22 (2012) 22840–22843.
- [30] J.E.D. Davies, *J. Inorg. Nucl. Chem.* 35 (1973) 1531–1534.
- [31] Y. Lei, G. Wang, S. Song, W. Fan, H. Zhang, *CrystEngComm* 11 (2009) 1857–1862.
- [32] E. Bandini, P. Beneventi, D. Bersani, R. Capelletti, M. Gospodinov, L. Kovacs, *Mikrochim. Acta Suppl.* 14 (1997) 489–490.
- [33] O.M. Bordun, *J. Appl. Spectrosc.* 64 (1997) 476–479.
- [34] A.V. Khomich, Y.F. Kargin, P.I. Perov, V.M. Skorikov, *Izv. Akad. Nauk SSSR Neorg. Mater.* 26 (1990) 1709–1711.
- [35] R. Shi, T.G. Xu, L.H. Yan, Y.F. Zhu, J. Zhou, *Catal. Sci. Technol.* 3 (2013) 1757–1764.
- [36] X. Xiao, R. Hu, C. Liu, C. Xing, X. Zuo, J. Nan, L. Wang, *Chem. Eng. J.* 225 (2013) 790–797.
- [37] T.L. Thompson, J.T. Yates, *Chem. Rev.* 106 (2006) 4428–4453.
- [38] Y. Muraoka, N. Takubo, Z. Hiroi, *J. Appl. Phys.* 105 (2009) 103702.
- [39] C. Zhang, Y.F. Zhu, *Chem. Mater.* 17 (2005) 3537–3545.
- [40] D. Liu, Y.H. Lv, M. Zhang, Y.F. Liu, Y.Y. Zhu, R.L. Zong, Y.F. Zhu, *J. Mater. Chem. A* 2 (2014) 15377–15388.